RSC Advances

PAPER

View Article Online
View Journal | View Issue

Cite this: *RSC Adv.*, 2025, **15**, 34537

Insight into the oxidase-mimicking activity enhancement of MnO_2 nanozymes by Co ion-doping for colorimetric sensor assays

Thi-Hien Pham,[a] Xuan-Dinh Ngo,[a] Nguyen Van Tuyen,[b] Chu Xuan Quang,[b] Pham-Cong De,[c] Tan Van Tran,*[d] Nguyen Pham Duy Linh,[e] Van-Tuan Hoang*[a] and Anh-Tuan Le*[a]

Manganese dioxide (MnO_2) nanomaterials have garnered significant attention as enzyme mimics due to their excellent catalytic properties. However, when applied to catalytic oxidation in biological systems, pure MnO_2 has shown limited performance. To address this limitation, we synthesized Co-doped MnO_2 nanoparticles with enhanced oxidase-mimicking activity through a facile chemical method. These Co–MnO_2 nanoparticles are characterized by the structural incorporation of Co ions into the MnO_2 lattice, likely substituting Mn sites, which crucially induces a high density of surface oxygen vacancies (OVs), a key factor for enhanced catalysis. The presence of these OVs, confirmed by XPS, alongside the introduction of Co, leads to modulated electronic configurations and promotes the active participation of Mn^{3+}/Mn^{4+} and Co^{2+}/Co^{3+} redox couples. This combination is believed to facilitate synergistic catalytic reactions and accelerated electron transfer during catalytic reactions. Co–MnO_2 nanoparticles demonstrated notable kinetic parameters toward the oxidation of 3,3′,5,5′-tetramethylbenzidine (TMB), exhibiting a low Michaelis–Menten constant (K_m = 1.17 mM) and an elevated maximum velocity (V_{max} = 4.69 × 10^{-6} M s^{-1}). UV-Vis spectroscopy and colorimetric analysis revealed a notably intensified chromogenic response at 650 nm for Co–MnO_2 systems. Leveraging these properties, a sensitive and reliable colorimetric platform was developed for ascorbic acid (AA) detection, achieving a broad linear range (2–100 μM) and a low detection limit (1.23 μM). The practical application of this colorimetric sensing platform was validated through successful testing with real samples, highlighting its potential for various colorimetric sensing applications.

Received 28th May 2025
Accepted 11th September 2025

DOI: 10.1039/d5ra03755g

rsc.li/rsc-advances

1. Introduction

Nanomaterials with enzyme-mimicking functions are progressively attracting significant attention from researchers worldwide due to their superior properties, such as electrical conductivity,[1] ion exchange,[2] optical properties,[3] and catalytic activity.[4] Various nanomaterials, including metal oxides, carbon nanomaterials, noble metals, and functional polymers, have been studied and developed as efficient nanozymes.[5–8] Despite their ability to withstand extreme environmental conditions and suitability for large-scale production, nanozymes still lag behind natural enzymes in terms of selectivity and catalytic activity. To address these limitations, researchers have developed various tuning strategies to maximize nanozyme activity, focusing on size, morphology, structure, ligand modification, heteroatom doping, and external stimuli. For instance, a hydrothermally synthesized $SnFe_2O_4$ nanozyme with catalase and glutathione peroxidase-like activity showed significant improvement after modification with poly(styrene)-*block*-poly(ethylene glycol) (pS-PEG).[9] Notably, the activity of carbon-based nanozymes can be enhanced by doping with Fe and N. Wang's team created a nanozyme material with a higher ID/IG intensity ratio than the undoped material by introducing N_2 heteroatoms into Q-graphene to generate N-doped surface defects.[10]

Designing and optimising nanozymes with enhanced catalytic performance represents a frontier in materials science research. These artificial enzyme mimics offer distinct advantages over their natural counterparts, including greater stability under harsh conditions, longer shelf life, and scalable production at lower costs. Metal oxide-based nanozymes, in particular, have emerged as promising candidates due to their tunable

[a]*Phenikaa University Nano Institute (PHENA), Phenikaa University, Hanoi 12116, Vietnam. E-mail: tuan.hoangvan@phenikaa-uni.edu.vn; tuan.leanh@phenikaa-uni.edu.vn*

[b]*Center for Advanced Materials and Environmental Technology, National Center for Technological Progress, Hanoi 12116, Vietnam*

[c]*Department of Nanoenergy Engineering and College of Nanoscience and Nanotechnology, Pusan National University, Busan 46241, Republic of Korea*

[d]*Faculty of Biotechnology, Chemical and Environmental Engineering (BCEE), Phenikaa University, Hanoi 12116, Vietnam. E-mail: tan.tranvan@phenikaa-uni.edu.vn*

[e]*Department of Applied Chemical Materials, School of Material Science and Engineering, Hanoi University of Science and Technology, Vietnam*

physicochemical properties and versatile surface chemistry.[11–13] Recent advances in synthetic methodologies and characterization techniques have enabled precise control over nanozyme architecture and functionality, opening avenues for their application in sensing, biomedicine, environmental remediation, and catalysis. The strategic incorporation of dopants into nanozyme structures presents an efficient approach for modulating catalytic activity. Dopants can significantly alter the host material's electronic properties, introduce crucial defect sites such as OVs, and modify surface reactivity, thereby enhancing substrate binding and conversion efficiency.[14]

Among metal oxides, manganese dioxide (MnO_2) is a cost-effective, environmentally friendly, and easily prepared material known for its intrinsic multi-enzyme mimetic activities.[15] The enzyme-like activity of MnO_2 is highly dependent on its structural properties, including crystalline phase, morphology, and surface characteristics such as OV. Many studies have been conducted to document that the properties of nanoparticles can be tuned by changing the synthesis method and modifying their surface, size, shape, and composition. MnO_2 nanomaterials with different morphologies (nanoparticles, nanoclusters, nanorods, nanowires, nanosheets,…) have been characterized for their oxidase activities. MnO_2 nanowires have the highest activity and stability for immunoglobulin binding applications.[16] For MnO_2 nanorods, Meng's group[12] modified different crystal structures, including α-, β-, and γ-MnO_2, through different fabrication methods. Using TMB as the substrate for the oxidation catalytic reaction, the results showed that β-MnO_2 nanorods exhibited the highest activity for applying glutathione (GSH) content detection. In a catalytic oxidation application for formaldehyde (HCHO) degradation, MnO_2 in the form of nanoparticles with a crystal structure in the γ-MnO_2 phase gave the best efficiency,[13] while in another study, γ-MnO_2 with a short nanorod structure achieved a lower HCHO removal efficiency than δ-MnO_2 in the flower-shaped form.[17] In addition to the influence of the morphology and crystal structure of single MnO_2, the oxidation activity of this nanozyme was also studied in doped and surface-modified materials.[18–20] Studies have shown that the catalytic oxidation efficiency of modified materials is higher than that of pristine MnO_2. Metal doping, especially transition metals (Fe, Co, Cu, Zn,…), is a key strategy to engineer the catalytic sites. Such doping can influence crystallinity, but more importantly, it is known to increase the amount of surface oxygen defects and modulate the availability of multiple metal valence states (*e.g.*, Mn^{3+}/Mn^{4+}, Co^{2+}/Co^{3+}), which can work synergistically to boost the oxidase activity of the material.

Beyond crystalline phase and morphology, the presence of OV is strongly correlated with the enzyme-like activity of MnO_2. These OVs are not mere imperfections; they are critical catalytic enhancers.[21,22] OVs can lower the band gap of MnO_2 and generate intermediate energy levels, accelerating electron transfer, which is crucial for catalytic reactions. They can also provide additional active sites for the adsorption and activation of reactants like molecular oxygen and the chromogenic substrate (*e.g.*, TMB), directly participating in or facilitating the catalytic turnover. Strategies to further enhance MnO_2 nanozyme activity include controlling its crystal structure and morphology, inducing structural changes like creating heterophase junctions, and doping with transition metals. Metal doping is a practical and effective approach to modulate the electronic or geometrical structure of metal oxides, often resulting in enhanced specific surface area, improved electronic conductivity, and, critically, promoting the formation of OVs.

Transition metal doping, specifically with elements like Fe, Cu, Zn, Ni, and Co, has been reported to significantly increase the amount of surface oxygen defects and improve the oxidase activity of MnO_2. Notable examples include Mo-doped MnO_2 nanoflowers synthesized *via* microwave-assisted hydrothermal methods, which exhibited enhanced enzyme-like activity and a stronger affinity for TMB compared to pure MnO_2.[23] Similarly, Sr-doped MnO_2 nanoflowers demonstrated significantly enhanced oxidase-like and laccase-like activities, which was attributed to increased OVs confirmed by EPR analysis.[24] Hydrothermally synthesized MnO_2 nanoflowers also showed enhanced oxidase-like catalytic activity, attributed to numerous active surface sites and the synergistic reaction between Cu^+/Cu^{2+} and Mn^{3+}/Mn^{4+} redox couples.[25]

Based on these successful examples, doping MnO_2 with other transition metals, such as Co, is a promising strategy to optimize its catalytic properties for specific applications further. Due to the similar ionic radii of Co and Mn ions, Co doping is expected to integrate effectively into the MnO_2 lattice without drastically altering its overall crystal structure or morphology at reasonable doping concentrations. Previous studies on Co-doped MnO_2 for other applications, such as magnesium ion storage, have shown that Co doping leads to a change in the coordination environment and is more oxygen-deficient than undoped MnO_2, generating abundant Ovs.[26] These OVs, confirmed by techniques like EPR and XPS, improve electronic conductivity, expose more active sites, and promote ion transport. While the primary focus of these studies was electrochemical performance, the demonstrated structural and electronic modifications – particularly the increase in OVs and enhanced conductivity, and the introduction of multivalent Co ions alongside Mn ions – are also highly relevant to and directly implicated in enhancing enzyme-mimicking catalytic activity.[27]

Inspired by these advancements, our study investigates Co-doped MnO_2 nanoparticles as high-performance nanozymes for colorimetric sensing applications. Using a facile chemical synthesis method, we aimed to create Co–MnO_2 nanoparticles with uniform size and enhanced oxidase activity. Based on these considerations, we hypothesize that Co doping into MnO_2 can induce a series of synergistic effects, including the successful substitution of Co ions into Mn lattice sites, leading to the creation of abundant OVs, modulation of the electronic structure, enhancement of electrical conductivity, an increased density of active catalytic sites, and improved substrate adsorption. Critically, we propose that these factors foster a synergistic catalytic mechanism involving both the OVs and the multivalent redox couples of Mn and Co. These modifications are anticipated to collectively accelerate reaction kinetics and enhance the oxidase-mimicking catalytic performance of MnO_2. The enhanced oxidase-like activity is effectively utilized

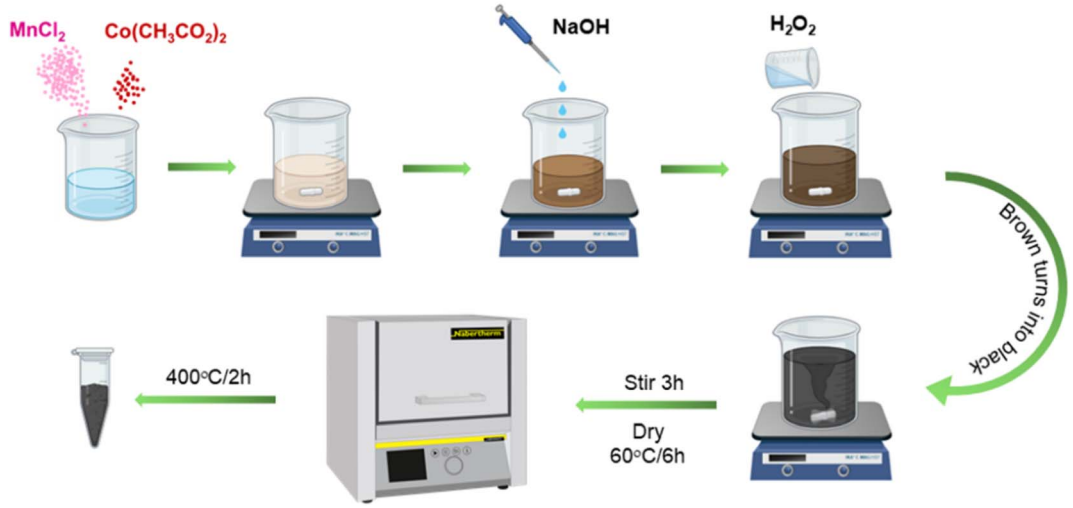

Scheme 1 Process synthesis of Co–MnO_2 nanoparticles.

for the sensitive colorimetric detection of AA using the Co–MnO_2 + TMB system as a probe. Our findings highlight the potential of Co-doped MnO_2 nanoparticles as a promising, cost-effective platform for developing sensitive colorimetric sensors for critical analytes like AA.

2. Experimental section

2.1. Chemicals

3,3′,5,5′-Tetramethylbenzidine (TMB) were purchased from Sigma-Aldrich (USA). Manganese(II) chloride tetrahydrate ($MnCl_2 \cdot 4H_2O$), Hydrogen peroxide (H_2O_2, 30%wt), sodium hydroxide (NaOH), cobalt(II) acetate tetrahydrate ($Co(CH_3CO_2)_2 \cdot 4H_2O$) and ascorbic acid (AA) were provided by Sinopharm Chemical Reagent Co., Ltd (China). In addition, the double-distilled water used in the process was prepared using a Mili-Q® system (18.2 MΩ cm at 25 °C). The phosphate-buffered saline (PBS) buffer solution (pH 7.3) was prepared by using NaCl, KCl, $Na_2HPO_4 \cdot 12H_2O$, and KH_2PO_4 (>99%, Merck KGaA, Germany). The pH of PBS buffer was adjusted by using HNO_3 (0.1 M) and NaOH (0.1 M). All chemicals were used as received without any further purification.

2.2. Synthesis of Co–MnO_2 nanoparticles

Co–MnO_2 nanoparticles were synthesized by a modified method.[28] First, 990 mg of $MnCl_2 \cdot 4H_2O$ and 8 mg of $Co(CH_3CO_2)_2 \cdot 4H_2O$ were dissolved in 100 mL of distilled water by magnetic stirring for 30 min. Next, 0.1 M NaOH solution was added dropwise and slowly until the brown suspension reached pH 9.0. The mixture was further stirred at room temperature for 30 min. Finally, 30%wt H_2O_2 was added until the solution turned black, indicating that Mn^{2+} had been oxidized to Mn^{4+}. The mixture was stirred for 3 h in the air at room temperature. At the end of the process, the solution was centrifuged and washed with distilled water several times to remove the residue and dried at 60 °C for 6 h. The resulting black powder was ground and calcined at a temperature of 400 °C for 2 h. After calcination, the resulting powder was stored in a dry, dark environment at room temperature prior to characterization and further use (Scheme 1). The samples were characterised using SEM, EDS Mapping, TGA, FTIR, XRD and UV-Vis methods.

2.3. The oxidase-mimicking activity of Co–MnO_2 nanoparticles

In this experiment, 1.2 mL of MnO_2 solution (0.02 mg mL^{-1}) was added with 2 mL of PBS buffer solution pH 4.0 and shaken well for 5 min. Finally, 0.4 mL of TMB (0.5 mM) was added and shaken again for 5 min to complete the reaction.

2.4. Selection of optimal conditions and kinetic analysis for the oxidase-mimicking reaction

To choose appropriate parameters for TMB oxidation by Co–MnO_2, conditions such as Co–MnO_2 nanozyme concentration, TMB substrate concentration, pH of reaction buffer solution and response time were inspected.

The kinetics of Co–MnO_2 material were evaluated by measuring the absorbance changes of the Co–MnO_2 + TMB system every 50 seconds. The kinetic parameters – Michaelis constant (K_m) and the maximum initial (V_{max}) were calculated through the Lineweaver–Burk equation:

$$\frac{1}{V} = \frac{K_m}{V_{max}}\left(\frac{1}{[S]} + \frac{1}{K_m}\right)$$

where V represents the initial velocity, V_{max} represents the maximum reaction velocity, K_m is the Michaelis–Menten constant, and $[S]$ is the TMB substrate concentration.

2.5. Application in colorimetric sensor assay for AA detection

2.5.1. Colorimetric assay. The experiment was performed similarly to experiment 2.4. However, the input parameters such as Co–MnO_2 material concentration, TMB substrate concentration and reaction environment temperature were

changed to optimize experimental conditions. The Co–MnO_2 – TMB system was used to detect AA with the change in absorbance at 650 nm wavelength as a function of AA concentration.

2.5.2. Detection of the AA in real sample. Oranges and tomatoes obtained from a local market were washed with distilled water, squeezed, and sonicated for 30 minutes. The resulting juice was centrifuged at 3000 rpm for 10 minutes. The supernatant was sifted through filter paper, collecting 5 mL of each sample. Vitamin C tablets purchased from a nearby pharmacy were pulverized. The powder was then thoroughly dissolved by sonicating 60 mg in 10 mL of distilled water for 30 minutes. The mixture was next filtered using filter paper to remove the ingredients that were not fully dissolved. Three crude extract samples were diluted fifty times with double-distilled water before being detected using the Co–MnO_2 + TMB method.

2.6. Characterization methods

The morphology of nanomaterial was studied by scanning electron microscopy (SEM) and energy dispersive X-ray spectrometry (EDS) mapping techniques (Hitachi S-4800, Japan). The crystal structures of synthesized nanomaterial were analyzed using an X-ray diffractometer (XRD Empyrean, PANalytical, Netherlands) with Cu Kα radiation in the 2θ range from 5° to 70°. Fourier transform infrared (FTIR) spectra were obtained using Nicolet iS10 FT-IR (Thermo Scientific, USA). The thermal properties of the materials were verified by TGA measurement (TGA/DSC 3+, Metler Toledo). Absorbance spectra were acquired using NANOCOLOR UV/VIS II Spectrophotometer (Macherey-Nagel, Germany). An XPS measurement was carried out using a Nexsa instrument from Thermo Fisher Scientific, equipped with an Al Kα (1486.6 eV) X-ray source (with 150 W anode power) under ultra high vacuum conditions of 10−9 mbar.

3. Results and discussion

3.1. Characterization of Co–MnO_2 nanoparticles

Fig. 1 illustrates the morphology and elemental distribution of Co–MnO_2 through SEM and EDS mapping. The SEM image reveals uniformly dispersed particles with consistent size distribution. The morphology of MnO_2 remains unchanged mainly after Co doping, suggesting that the introduction of cobalt ions does not significantly alter the growth mechanism or particle formation (Fig. 1A). Fig. 1B presents an overlay of the EDS maps, providing visual confirmation of the elemental composition and spatial distribution within the Co–MnO_2 material. The color-coded mapping shows the distribution of oxygen (O), manganese (Mn), and cobalt (Co), with overlapping signals indicating regions where these elements coexist (Fig. 1C). The consistent and uniform presence of the Co signal throughout the mapped area confirms the successful incorporation of cobalt into the MnO_2 matrix without segregation or formation of separate cobalt oxide phases. The EDS spectrum showed that the present of Mn and Co within the as-synthesized sample (Fig. S1), consistent with both the input mass ratio of Mn^{2+} and Co^{2+} salts and the previously published result.[29]

This homogeneous distribution of cobalt within the MnO_2 structure is crucial for enhancing the catalytic properties, as it ensures that the electronic and structural modifications

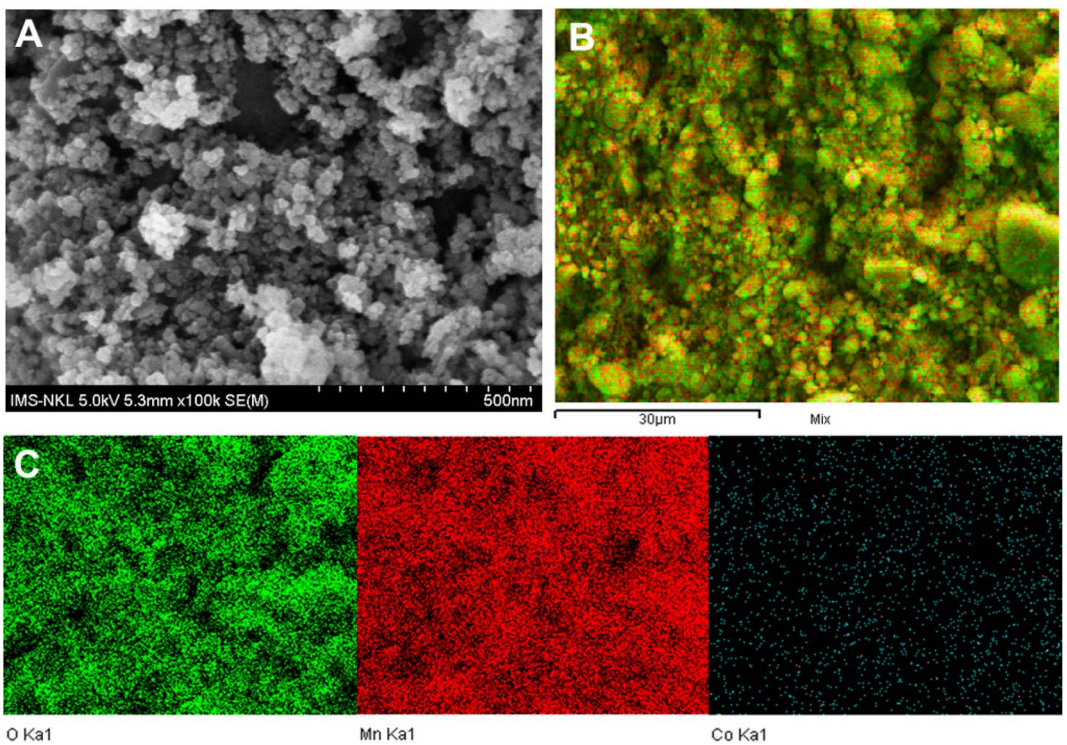

Fig. 1 SEM (A) and EDS Mapping (B and C) of Co–MnO_2 nanoparticles.

induced by Co doping occur uniformly throughout the material. The even distribution of dopants typically leads to a more consistent catalytic performance by creating a uniform distribution of active sites across the nanozyme surface. Furthermore, the preserved particle morphology with added Co doping suggests that the enhanced catalytic activity observed in Co–MnO_2 likely stems from electronic and structural modifications rather than morphological changes.

Fig. 2 presents a comprehensive set of characterization data for the synthesized Co–MnO_2 nanoparticles, providing insights into its structural, compositional, and surface chemical properties. The XRD patternin Fig. 2A provides crucial information regarding the crystal structure and phase purity of the Co–MnO_2 nanoparticles. The presence of distinct diffraction peaks indicates the crystalline nature of the synthesized material. Observation of the diffraction pattern shows the appearance of characteristic diffraction peaks of α-MnO_2 material (JCPDS 44-0141) at 18°, 28.7°, 32.4°, 36.5°, 42.4°, 56.4° and 60.1° corresponding to the crystal planes (200), (310), (101), (211), (301), (600), and (251), respectively. Fig. S2 provides a simulated structure of Co–MnO_2 nanoparticles based on XRD data, illustrating the structural arrangement of Co atoms within the MnO_2 framework.

Doping does not fundamentally alter the crystalline structure of MnO_2, but it does enhance the material's crystallinity, as evidenced by the increase in intensity of the relevant diffraction peaks when compared to the diffraction pattern of the undoped MnO_2 sample.[30] The absence of additional peaks corresponding to cobalt oxides suggests the successful incorporation of cobalt ions into the MnO_2 lattice rather than forming a separate phase at this doping level. This integration is likely facilitated by the comparable (though not identical) ionic radii of Co ions (which can exist as Co^{2+} or Co^{3+}) and Mn ions (primarily Mn^{4+} in MnO_2, with some potential Mn^{3+}),[31] allowing Co to effectively substitute specifically at the Mn octahedral sites within the MnO_2 crystal framework.[32] This substitution occurs without drastically altering its overall crystal arrangement at the utilized doping concentration. By applying the Scherrer equation to the whole width at half maximum of the (211) plane, the crystallite size of the Co–MnO_2 sample was determined to be approximately 11 nm, indicating the nanocrystalline nature of the synthesized material. This enhanced crystallinity observed in the Co-doped sample may contribute to the improved catalytic properties, as better-defined crystal structures often provide more effective electron transfer pathways crucial for oxidase-like activity. Furthermore, incorporating Co into the MnO_2 lattice (specifically, the substitution of Mn^{4+} by lower-valence Co ions like Co^{2+} or Co^{3+}) likely creates significant local coordination environment changes, induces lattice strain, and necessitates charge compensation mechanisms. These mechanisms primarily include the generation of oxygen deficiencies (OV) and potentially the modulation of oxidation states in adjacent Mn ions (*e.g.*, reduction of some Mn^{4+} to Mn^{3+}).[33] These resultant OVs and altered electronic structures are vital for enhanced catalytic performance, as supported by previous studies on transition metal-doped MnO_2 systems.

The FTIR spectrum shown in Fig. 2B reveals the vibrational modes of the chemical bonds present in the Co–MnO_2 sample, providing insights into the functional groups and structural characteristics of the synthesized material. Two strong characteristic peaks observed at 526 cm^{-1} and 615 cm^{-1} are attributed to the stretching vibrations of the Mn–O bond in the MnO_6 octahedra network along the double chains of α-MnO_2.[6] These peaks confirm the formation of the MnO_2 framework in the synthesized material. The bands observed in the range of 400–700 cm^{-1} further reveal the presence of the MnO_6 octahedral structure. Weaker bands at 1112 cm^{-1} and 1405 cm^{-1} correspond to the metal bond vibration (M-O-M) and the stretching vibration of the carboxyl acetate group (C═O), respectively.[30,31] The presence of symmetric and asymmetric stretching

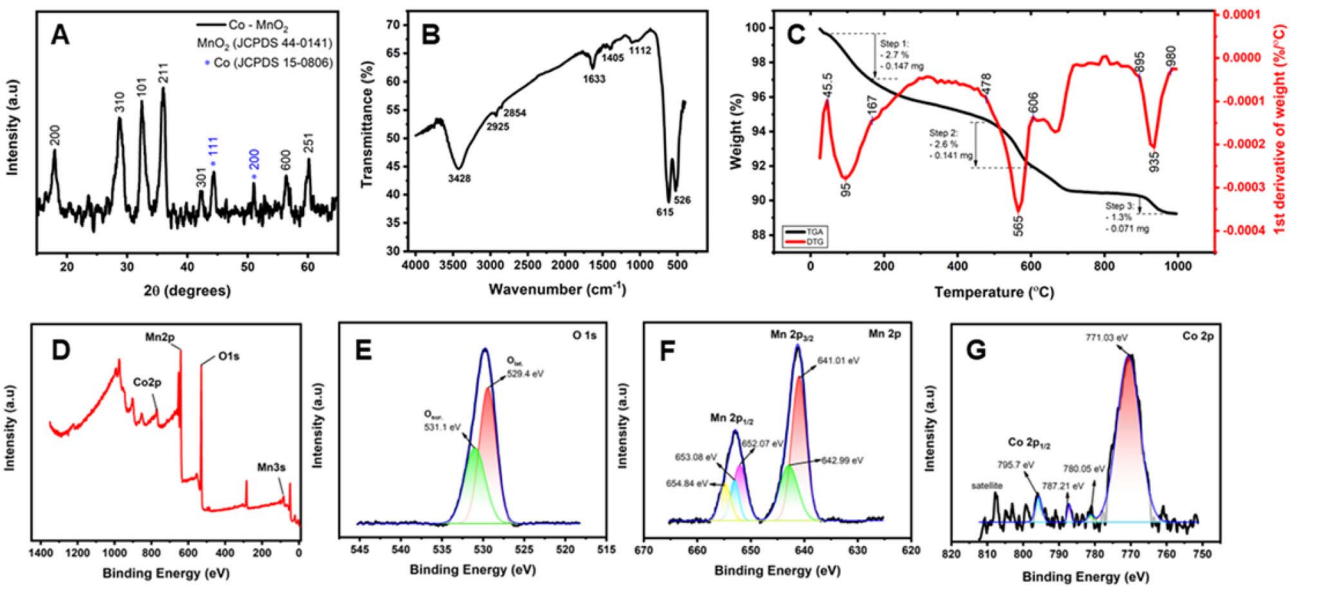

Fig. 2 (A) XRD and (B) FTIR spectrum, (C) TGA and DTG curve of Co–MnO_2 nanoparticles, and (D–G) XPS spectra of Co–MnO_2 nanoparticles.

vibrations in the C–H bond is evidenced by the vibrational modes at 2854 cm^{-1} and 2925 cm^{-1}.[30] The spectrum also shows prominent peaks at 1633 cm^{-1} and 3428 cm^{-1}, which indicate bending and stretching vibrations of hydroxyl groups from water molecules on the sample surface. The bands observed in the range of 700–3500 cm^{-1} can be attributed to vibrations caused by the interaction of Mn with Co metal ions and various functional groups, including OH, O, H, and C. The overall FTIR profile confirms the successful synthesis of manganese cobalt nanoparticles with the expected α-MnO_2 structure. Subtle shifts in the position and intensity of the Mn–O bands compared to pure MnO_2 may indicate the influence of cobalt ions on the vibrational modes of the MnO_2 lattice, further supporting the successful incorporation of Co into the MnO_2 framework.[34]

The TGA and DTG curves depicted in Fig. 2C illustrate the thermal stability and decomposition profile of the Co–MnO_2 material as a function of temperature. The thermogravimetric analysis (TGA) of the Co–MnO_2 sample was performed in the temperature range of 25 to 1000 °C, providing valuable insights into the material's thermal behavior and phase transformations. The thermogram reveals that the Co–MnO_2 material exhibits relatively good thermal stability, with three distinct mass loss events totalling less than 15% of the initial mass. The primary thermal loss occurs below 200 °C and corresponds to the evaporation of adsorbed water molecules and the thermal decomposition of surface functional groups such as carboxyl and hydroxyl groups. This initial weight loss is characteristic of manganese oxide materials, which typically contain surface-bound water molecules. The second thermal event, observed as a distinct peak at approximately 565 °C with a weight loss of 2.6%, can be attributed to the melting of MnO_2 (478 °C) and the subsequent crystallization of Mn_2O_3 (606 °C). This phase transformation is a critical thermal characteristic of manganese oxide materials and provides information about the structural stability of the synthesized Co–MnO_2. A third thermal peak is identified in the range of 895–980 °C, corresponding to a weight loss of approximately 1.3%. This event is ascribed to the phase transition or formation of the Mn_3O_4 structure.[35] The DTG curve exhibits clear peaks at these transition temperatures, confirming the discrete nature of these thermal events. The overall thermal profile of Co–MnO_2 demonstrates its stability at moderate temperatures, making it suitable for applications under varied thermal conditions.

The XPS spectra in Fig. 2D–G provides detailed information about the surface elemental composition and the oxidation states of the constituent elements in the Co–MnO_2 material. The full spectrum data shown in Fig. 2D confirms the presence of four elements – Mn, Co, and O – which align with the findings from both XRD and EDS characterization. Analysis of the high-resolution O 1 s spectrum (Fig. 2E) is paramount for understanding the nature and influence of surface oxygen species, particularly OVs, which are widely recognized as pivotal for the catalytic activity of metal oxides. The O 1 s spectrum of Co–MnO_2 can be deconvoluted into two main peaks. The peak at the lowest binding energy (approximately 529.4 eV) corresponds to lattice oxygen (O_{Lat}) in the Mn–O–Mn bonds of the MnO_2 framework. A distinct peak at an intermediate binding energy (around 531.1 eV) is attributed to oxygen in defect-rich sites or OV. The intensity and relative area of this OV peak are critical, as a higher concentration of Ovs (O_{ads}/O_{total} ~0.33), often induced by aliovalent doping like the incorporation of Co into the MnO_2 lattice, directly correlates with enhanced catalytic performance.[23,33]

The Mn 2p spectrum (Fig. 2F) is crucial for determining the multiple oxidation state of manganese in the Co–MnO_2 sample and understanding its role in synergistic redox reactions. The spectrum consists of two main spin–orbit split peaks, Mn $2p_{3/2}$ and Mn $2p_{1/2}$, with a characteristic energy separation. By fitting, we obtained Mn^{2+} (640.05 eV and 652.07 eV), Mn^{3+} (641.01 eV and 653.08 eV), and Mn^{4+} (642.99 eV and 654.84 eV), indicating the coexistence of three chemical valence states.[36] Further analysis was conducted on the Mn 3 s spectrum (Fig. S3), which exhibits multiplet splitting into two distinct peaks at 83.08 eV and 88.06 eV. Using the energy separation between these peaks (ΔE_{3S}), the average manganese valence (V_{Mn}) was calculated to be +3.43 according to the linear equation $V_{Mn} = 7.875 - 0.893\Delta E_{3S}$.[37] This value is significantly lower than the theoretical +4.0 for pure MnO_2, confirming that Co-doping induces the formation of Mn^{3+} ions as part of a charge compensation mechanism likely involving oxygen vacancies.

The Co 2p spectrum (Fig. 2G) provides information about the oxidation state and chemical environment of cobalt in the Co–MnO_2 material. Like Mn 2p, the Co 2p spectrum also exhibits splitting into Co $2p_{3/2}$ and Co $2p_{1/2}$ peaks, along with characteristic satellite peaks. Given the trace Co doping (low concentration as confirmed by EDX), the Co signal is weak and overlaps with matrix effects, making precise oxidation state assignment challenging from this spectrum alone. However, based on the overall XPS data (*e.g.*, Mn 2p showing mixed Mn^{3+}/Mn^{4+} states) and literature on similar Co-doped MnO_2 systems, we infer the presence of Co redox pairs contributing to enhanced catalysis.[38]

Furthermore, the presence of multiple oxidation states for both manganese (Mn^{2+}, Mn^{3+}, Mn^{4+}) and cobalt (Co^{2+}, Co^{3+}) within a single Co–MnO_2 material suggests the potential for synergistic redox reactions similar in principle to those observed in $CuMnO_2$ nanoflowers.[25] In the Co–MnO_2 system, it's hypothesized that electron transfer could occur between the different oxidation states of Mn, the different oxidation states of Co, and also between Mn and Co species. A potential synergistic pathway in Co–MnO_2 for its oxidase-like activity could involve several steps. Initially, molecular oxygen (O_2) might be activated by accepting electrons from the lower oxidation states of the metals, such as Co^{2+} and Mn^{3+} (or even Mn^{2+} if present and reactive), leading to their oxidation to Co^{3+} and Mn^{4+} respectively, and the formation of superoxide radicals ($O_2^{\bullet-}$). These superoxide radicals could then participate in further reactions, potentially leading to the generation of other reactive oxygen species (ROS) like hydrogen peroxide (H_2O_2) and hydroxyl radicals ($OH^{\bullet}$). Subsequently, these ROS, or the higher oxidation states of the metals (Co^{3+}, Mn^{4+}) directly, would then oxidize the chromogenic substrate (*e.g.*, TMB). During this substrate oxidation, the metal ions (Co^{3+}, Mn^{4+}) would be reduced back to their lower oxidation states (Co^{2+}, Mn^{3+}), allowing them to participate in further catalytic cycles. The underlying idea is

that having multiple metal centers in variable oxidation states within a material can facilitate these complex electron transfer pathways and ROS generation loops necessary for catalysis, leading to a synergistic effect that enhances overall activity. This interplay between the Co and Mn redox couples (Co^{2+}/Co^{3+} and $Mn^{2+}/Mn^{3+}/Mn^{4+}$), potentially mediated by OVs which can act as electron relays or sites for O_2 adsorption/activation, could therefore create a more complex and decidedly more active catalytic site compared to materials containing only one of these metals or fewer oxidation states. This enhanced catalytic turnover rate is crucial for the sensitivity and efficiency of Co–MnO_2 as an oxidase mimic in colorimetric sensing applications.

3.2. The oxidase-mimicking activity of Co–MnO_2 nanoparticles

Fig. 3 presents UV-Vis spectra and corresponding photographs (inset) of MnO_2, MnO_2 + TMB, Co–MnO_2, and Co–MnO_2 + TMB. The addition of the TMB substrate to the MnO_2 sample resulted in a discernible color change from colorless to blue in the inset photograph, visually confirming the oxidation of TMB by MnO_2 in an acidic atmosphere. This observation is corroborated by the UV-Vis spectrum for MnO_2 + TMB, which exhibits increased absorbance at 650 nm, a characteristic absorption wavelength for the blue oxidized form of TMB (TMB diamine complex). The absorbance at 370 nm, also associated with the TMB diamine, and a potential minor peak at 450 nm (TMB diimine) further support this finding.[35] Similarly, the reaction of Co–MnO_2 with TMB also led to a blue coloration in the corresponding photograph, indicating that Co–MnO_2 also possesses intrinsic oxidase-like catalytic activity capable of oxidizing TMB. The UV-Vis spectrum for Co–MnO_2 + TMB shows enhanced absorbance at 650 nm compared to Co–MnO_2 alone, confirming the formation of oxidized TMB.

Crucially, adding cobalt metal atoms to the MnO_2 lattice raises the catalytic activity of the material. This enhancement is visually evident when comparing the intensity of the blue color in the photographs of MnO_2 + TMB and Co–MnO_2 + TMB. The Co–MnO_2 + TMB solution exhibits a deeper blue color, suggesting a higher concentration of oxidized TMB. This qualitative observation is quantitatively supported by the UV-Vis spectra in Fig. 3, where the absorbance intensity at 650 nm for Co–MnO_2 + TMB is demonstrably higher than that for MnO_2 + TMB. This increased absorbance signifies a greater extent of TMB oxidation catalyzed by Co–MnO_2 within the same reaction time, thus confirming the enhanced oxidase-like activity upon cobalt doping.

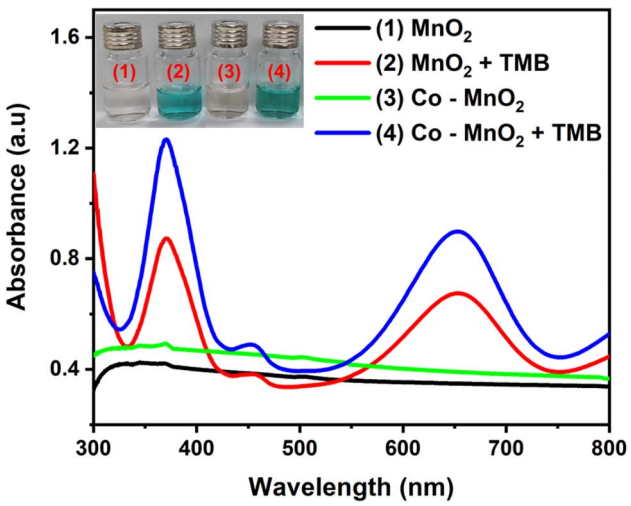

Fig. 3 Absorption spectra and photographs (inset) of (1) MnO_2, (2) MnO_2 + TMB, (3) Co–MnO_2 and (4) Co–MnO_2 + TMB.

The mechanism of TMB oxidation by MnO_2-based materials involves the redox properties of manganese ions, particularly the interconversion between Mn^{3+} and Mn^{4+} states, which facilitate electron transfer from TMB to oxygen. Co doping does not change the intrinsic catalytic activity type but rather elevates it. The observed increase in activity with Co doping could be attributed to a combination of beneficial factors stemming from the successful incorporation of Co into the MnO_2 lattice, as discussed in the characterization section. Foremost among these is the increased concentration of surface OVs resulting from Co doping, as clearly demonstrated by the XPS analysis (Fig. 2E). These additional OVs function as active sites for both O_2 adsorption/activation and substrate interaction, effectively accelerating the reaction rate.

The modulation of the electronic structure through the introduction of multivalent Co ions (Co^{2+}/Co^{3+}) alongside existing Mn redox states (Mn^{3+}/Mn^{4+}, and potentially Mn^{2+}) creates a more sophisticated and efficient electronic environment that facilitates critical electron transfer processes throughout the catalytic cycle. Perhaps the most significant contributor to the enhanced performance is the synergistic effect between the doped cobalt ions and the manganese redox couples within the MnO_2 lattice. This synergy, which is promoted by the OVs, enables more efficient oxygen activation and accelerated TMB oxidation through multi-step electron transfer pathways, ultimately resulting in the superior catalytic performance we observed. Fig. 3 confirms that both MnO_2 and Co–MnO_2 exhibit oxidase-like activity by oxidizing TMB, with comparative spectral analysis demonstrating that cobalt doping significantly enhances this catalytic performance, expanding potential applications in colorimetric sensing and catalysis.

3.3. The oxidase-mimicking reaction of Co–MnO_2 nanoparticles

3.3.1. Selection of optimal conditions. Fig. 4 presents the optimization of the oxidase mimetic activity of Co–MnO_2 by investigating the influence of various reaction parameters. Regarding the influence of the catalyst concentration, our investigation, with Co–MnO_2 concentrations ranging from 5 to 30 μg mL^{-1}, revealed a direct correlation between the catalyst concentration and the catalytic activity of Co–MnO_2 (Fig. 4A). As the concentration of Co–MnO_2 increased, the rate of TMB oxidation, indicated by the change in absorbance, also increased. The catalytic reaction system, as observed through absorption intensity and color stability at 370 nm, 450 nm, and 650 nm, reached a steady state after the Co–MnO_2 concentration attained 20 μg mL^{-1} (Fig. S4). This stabilization suggests

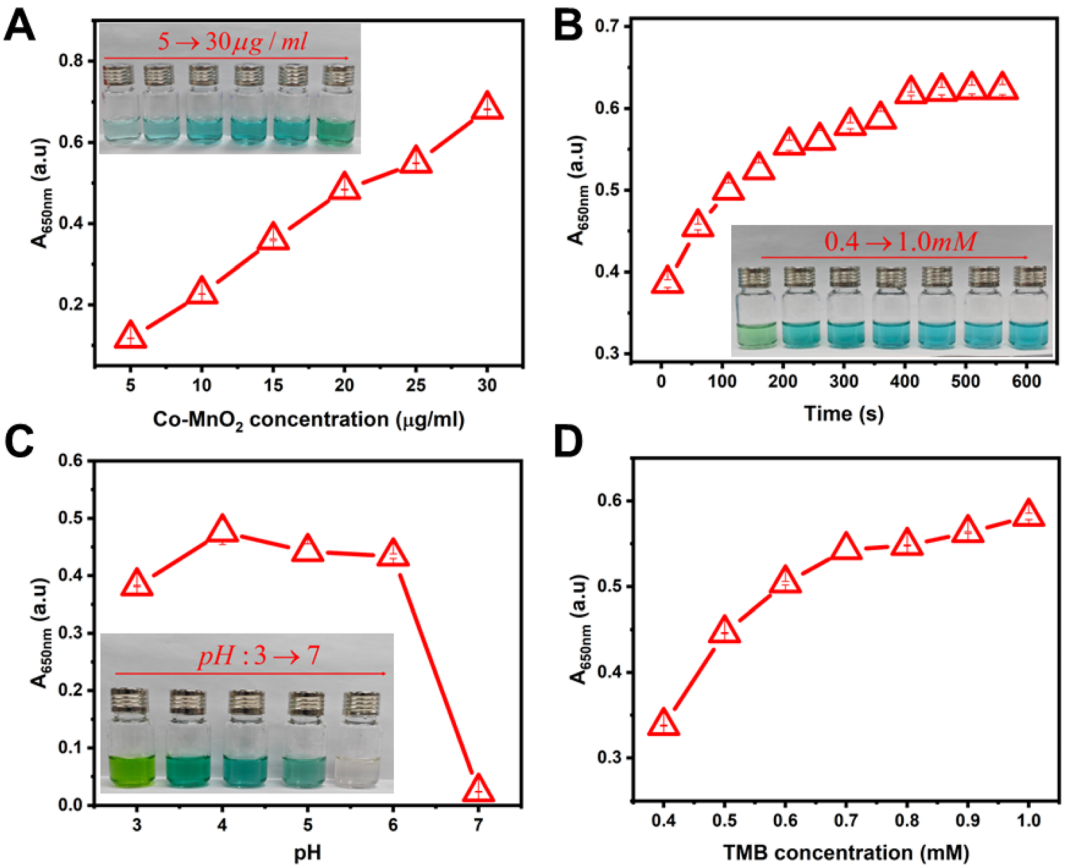

Fig. 4 Oxidase mimetic activity of the Co–MnO_2 is based on (A) concentration of Co–MnO_2, (B) concentration of TMB, (C) pH, and (D) time. Error bars are for 3 replicates ($n = 3$).

that at concentrations beyond 20 μg mL^{-1}, the increase in active sites does not proportionally enhance the reaction rate, potentially due to substrate availability or other limiting factors. Consequently, a Co–MnO_2 concentration of 20 μg mL^{-1} was determined to be optimal for subsequent assays, ensuring sufficient catalytic activity without excessive use of the material. This is consistent with observations in other nanozyme systems where an optimal catalyst concentration is crucial for efficient substrate conversion.

Furthermore, the impact of the TMB substrate concentration on the catalytic activity of Co–MnO_2 was systematically examined, as depicted in Fig. 4B. The results indicated that catalytic activity generally increased with increasing TMB concentration. As previously described, the oxidation of the colourless TMB substrate proceeds through intermediate oxidation complex products absorbing at 370 nm and 650 nm (blue), eventually leading to the fully oxidized form, oxTMB, absorbing at 450 nm (yellow).[35] Our findings showed that when the TMB concentration was below 0.5 mM, the concentration of the immobilized Co–MnO_2 material appeared to become a limiting factor, resulting in a relatively low absorption intensity at 650 nm (incomplete formation of the blue intermediate) and a significant rise at 450 nm (over-oxidation to the yellow diimine form) (Fig. S6A). This suggests an imbalance where a surplus of catalytic sites relative to substrate molecules leads to rapid and complete oxidation. However, the system demonstrated stability at a TMB concentration of 0.5 mM, evidenced by a slight and uniform increase in absorbance across all three wavelength regions (370, 450, and 650 nm) with further increases in TMB concentration up to 1.0 mM (Fig. S6B). This suggests that at 0.5 mM TMB, a suitable equilibrium is established between substrate availability and the concentration of active catalytic sites on the Co–MnO_2 surface, allowing for efficient and controlled oxidation. Therefore, a TMB concentration of 0.5 mM was identified as the ideal concentration for further research, providing a balance between reaction rate and selectivity for the desired oxidation state of TMB.

The influence of the reaction medium's pH was thoroughly investigated to optimize the Co–MnO_2 + TMB catalyst system. Our experiments revealed that the color reaction between Co–MnO_2 and TMB occurs exclusively under acidic conditions, with no observable reaction in neutral to alkaline environments (Fig. 4C). This pH dependency aligns with findings reported for similar metal-doped MnO_2 systems, particularly the $CuMnO_2$-TMB system, which also demonstrated reactivity only in acidic media. In the highly acidic range (pH 3), the catalytic reaction proved excessively strong, resulting in disproportionately high absorption at the 450 nm peak, which negatively impacted the controlled color development of TMB. The 4, 5, and 6 pH values produced comparable color intensity and absorption

characteristics (Fig. S5). However, detailed analysis revealed that pH 4 provided the most optimal conditions for the catalytic reaction, offering an ideal balance between reaction rate and controlled color development. This optimal pH determination at 4 is consistent with previous studies,[32,37,38] which similarly identified moderate acidic conditions as ideal for oxidase-like reactions involving manganese dioxide-based nanozymes. The pH dependency observed can be attributed to the influence of hydrogen ion concentration on both the surface charge of the Co–MnO_2 nanoparticles and the protonation state of TMB. These factors significantly impact the adsorption and subsequent oxidation of the substrate at the catalyst surface.

The interaction time between the reactants in the Co–MnO_2 + TMB system was also a critical parameter studied. The results demonstrated that the catalytic activity of the system increased with response time from 10 to 500 seconds. This is expected as a longer reaction time allows for more substrate molecules to interact with the catalytic sites on the Co–MnO_2 material, leading to increased product formation. However, as shown in Fig. 4D, the absorption progressively stabilized after 5 minutes (300 seconds) of reaction, indicating that the reaction reached a near steady-state. Considering the balance and potential reciprocal influence of other reaction parameters, a response time of five minutes was chosen for further studies. This suggests that while longer times lead to slightly increased product formation, a five-minute reaction time provides a good compromise for achieving sufficient and stable catalytic activity for subsequent experiments, likely preventing unnecessary delays without significant loss of signal intensity.

3.3.2. Kinetic analysis of Co–MnO_2 nanoparticles. Steady-state kinetic studies were conducted to evaluate their oxidase-like activity using TMB as the substrate. The enzymatic reaction rates were measured as a function of TMB concentration, and the kinetic parameters, specifically the K_m and V_{max}, were determined by fitting the data to the Michaelis–Menten model. The Lineweaver–Burk plots, derived by plotting the inverse of the reaction velocity against the inverse of the substrate concentration (as shown in Fig. 5), provided linear relationships that facilitated the accurate calculation of these parameters.

The K_m is a crucial parameter that reflects the affinity of the enzyme (in this case, the nanozyme) for its substrate (TMB). A lower K_m value indicates a higher affinity, meaning that the enzyme can achieve half of its maximum velocity at a lower substrate concentration. Our results show that the Co–MnO_2 nanozyme exhibited a lower K_m value (1.17 mM) than the undoped MnO_2 (1.81 mM).[35] This observation suggests that incorporating cobalt (Co) into the MnO_2 matrix enhances the binding affinity of the nanozyme towards the TMB substrate. This stronger affinity likely facilitates the initial interaction and subsequent oxidation of TMB by the Co–MnO_2 nanozyme. The maximum initial velocity (V_{max}) represents the highest rate at which the enzyme can catalyze the reaction when the substrate concentration is saturating. A higher V_{max} value signifies a greater catalytic activity. The kinetic data revealed that the Co–MnO_2 nanozyme displayed a higher V_{max} (4.69×10^{-6} M s^{-1}) than the undoped MnO_2 (3.88×10^{-6} M s^{-1}).[35] This clearly demonstrates that the doping of Co significantly enhances the catalytic performance of the MnO_2 nanozyme for TMB oxidation. The increased V_{max} indicates a faster substrate turnover rate to the oxidized product (oxTMB) by the Co–MnO_2 nanozyme under optimal conditions. This is consistent with the observation that metal doping in MnO_2 also resulted in enhanced enzyme-like activity.

The enhanced catalytic performance of the Co–MnO_2 nanozyme, as evidenced by the lower K_m and higher V_{max} values, highlights the beneficial effect of heteroatom doping on the oxidase-like activity of MnO_2. These improved kinetic parameters are consistent with the proposed mechanisms discussed in Section 3.1. Firstly, introducing Co ions into the MnO_2 lattice may alter the electronic structure of the material, potentially

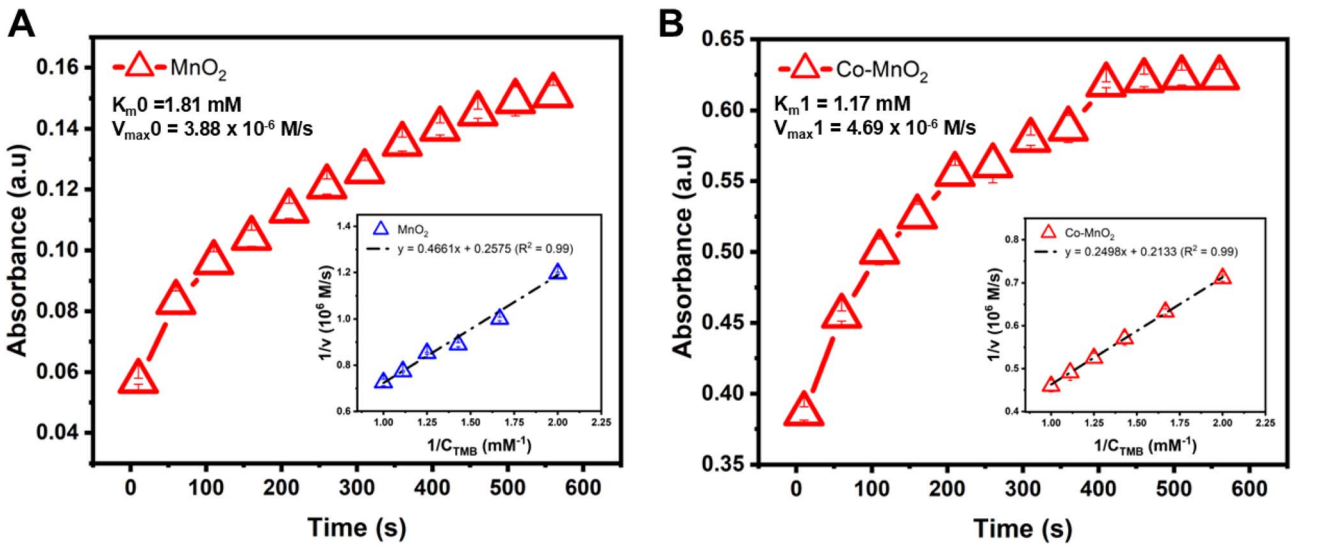

Fig. 5 Plot of absorbance at 650 nm peak *versus* time of the systems (A) MnO_2 + TMB and (B) Co–MnO_2 + TMB, and Lineweaver–Burk plot (inset), respectively.

creating more active sites or enhancing the redox properties necessary for TMB oxidation. Studies on Mo-doped MnO_2 have suggested that doping can increase the specific surface area and reduce charge transfer resistance, thereby improving catalytic properties.[23] Similar effects might be at play with Co doping. Secondly, the doping process could increase the concentration of surface OVs. It is well-established that the enzyme-like activity of MnO_2 is highly correlated with its surface OVs, which can facilitate electron transfer during the catalytic process. The observed enhancement in OV content through Co doping is corroborated by XPS findings reported in previous literature.[26] This increase in OVs in Co–MnO_2 could provide more active sites for the adsorption and activation of both oxygen and the TMB substrate, leading to a higher reaction rate and stronger substrate affinity. Furthermore, the synergistic interplay between the multiple oxidation states of Co and Mn (Co^{2+}/Co^{3+}, $Mn^{2+}/Mn^{3+}/Mn^{4+}$), facilitated by these OVs, provides more efficient electron transfer pathways, directly contributing to the accelerated reaction kinetics (higher V_{max}) and potentially influencing substrate binding affinity (K_m).

Comparing our findings with kinetic parameters reported for other MnO_2-based nanozymes can provide further context. For instance, one study reported a K_m of 1.612 mM and a V_{max} of 6.12×10^{-8} M s^{-1} for *r*-MnO_2/β-MnO_2 heterophase nanozymes,[35] and another cited a K_m of 0.0011 mM and a V_{max} of 30×10^{-8} M.S^{-1} for MnO_2.[26] It is important to note that these values can vary significantly depending on the specific morphology, crystal structure, and synthesis method of the MnO_2 material. However, our results indicate that Co doping can be a facile strategy to modulate the kinetic parameters of MnO_2, leading to enhanced oxidase-like activity with a higher affinity for the TMB substrate and a faster maximum reaction rate. This improvement underscores the potential of Co–MnO_2 nanozymes for applications in colorimetric sensing and other catalytic processes that rely on efficient TMB oxidation. For a broader comparison, the kinetic parameters of our Co–MnO_2 nanozyme alongside other recently reported MnO_2/Co-based nanozymes are summarized in Table S1, highlighting the competitive performance of our material.

3.4. Colorimetric sensor assay for AA detection

3.4.1. Sensitivity test. Based on the established oxidase-mimicking activity enhancement of the Co–MnO_2 nanozyme with TMB, a colorimetric probe was developed to detect AA. This detection strategy capitalizes on the principle that AA acts as an inhibitor of the Co–MnO_2 catalytic activity. Specifically, AA reacts with Mn^{4+} in the Co–MnO_2 nanozyme, leading to the formation of dehydroascorbic acid (DHAA) and Mn^{2+}, thereby reducing the amount of active Mn^{4+} species available for TMB oxidation and consequently decreasing the production of the blue-colored oxidized TMB (oxTMB). In Co–MnO_2/TMB/AA system, the mechanism can be described by the following reactions:

Oxidation of TMB by Mn^{4+} in Co–MnO_2:

$$\text{TMB (colorless)} + Mn^{4+} \rightarrow \text{oxTMB (blue)} + Mn^{2+}$$

Reduction of Mn^{4+} by AA:

$$C_6H_8O_6\ (AA) + 2Mn^{4+} \rightarrow C_6H_6O_6\ (DHAA) + 2Mn^{2+} + 2H$$

In the presence of AA, part of the Mn^{4+} is consumed to generate DHAA and Mn^{2+}, reducing the amount of Mn^{4+} available for TMB oxidation. As a result, the production of oxTMB decreases, and the color intensity diminishes proportionally with the AA concentration.

To quantify this inhibitory effect, the change in absorbance at 650 nm (ΔA) was monitored using the formula $\Delta A = A_0 - A_{650}$, where A_0 represents the initial absorbance of the Co–MnO_2 + TMB system in the absence of AA, and A_{650} is the absorbance observed after the addition of AA. As depicted in Fig. 6A, a steady decrease in the absorbance value and a concomitant fading of the blue color were observed with increasing concentrations of AA from 0 μM to 300 μM. This visual and spectrophotometric observation confirms the inhibitory effect of AA on the oxidase-like activity of the Co–MnO_2 nanozyme.

Further analysis of the absorbance changes revealed a near-linear correlation between the ΔA value and the AA concentration within the lower concentration range of 2 μM to 100 μM. This linear relationship (Fig. 6B and C) is crucial for quantitative colorimetric detection. Based on this linear range, the estimated limit of detection (LOD) for AA was calculated to be 1.23 μM using the $3.3\sigma/S$ criterion, where S is the slope of the linear calibration curve and σ is the standard deviation of the measurements. This LOD indicates the high sensitivity of the developed Co–MnO_2-based colorimetric probe for AA detection. In contrast, the undoped MnO_2 showed inferior performance, with a narrower detection range (4–100 μM) and a higher detection limit of 3.04 μM (Fig. S7), highlighting the clear advantage of Co-doping.

The observed inhibitory mechanism, where AA reduces Mn^{4+} to Mn^{2+}, is consistent with previous studies on MnO_2-based nanozymes for AA detection. Multiple research groups have reported similar sensing mechanisms. In studies of *r*-MnO_2/β-MnO_2 heterophase nanostructures, researchers demonstrated that MnO_2 with oxidase-like activity could be reduced to Mn^{2+} by AA, inhibiting TMB oxidation. The Mo–MnO_2 nanozyme system similarly exhibited suppressed color development when exposed to AA, indicating comparable redox interactions. $CuMnO_2$ nanoflowers have also been shown to facilitate the reduction of blue oxTMB back to colorless TMB upon AA addition. These consistent findings across various metal-doped MnO_2 systems suggest a common sensing mechanism based on the competitive redox reaction between AA and the manganese oxide catalyst, which forms the foundation for quantitative colorimetric detection methods.

The achieved limit of detection of 1.23 μM for AA using the Co–MnO_2 + TMB system demonstrates its potential for sensitive detection. While a direct comparison of LOD values with other studies is complex due to varying experimental conditions and nanozyme characteristics, it is worth noting that other MnO_2-based nanozymes have also shown comparable or even lower LODs for AA detection. For instance, *r*-MnO_2/β-MnO_2 heterophase nanostructures achieved an LOD of 0.84 μM, and MnO_2 nanosheets reported an LOD of 0.06 μM. However, the Co-

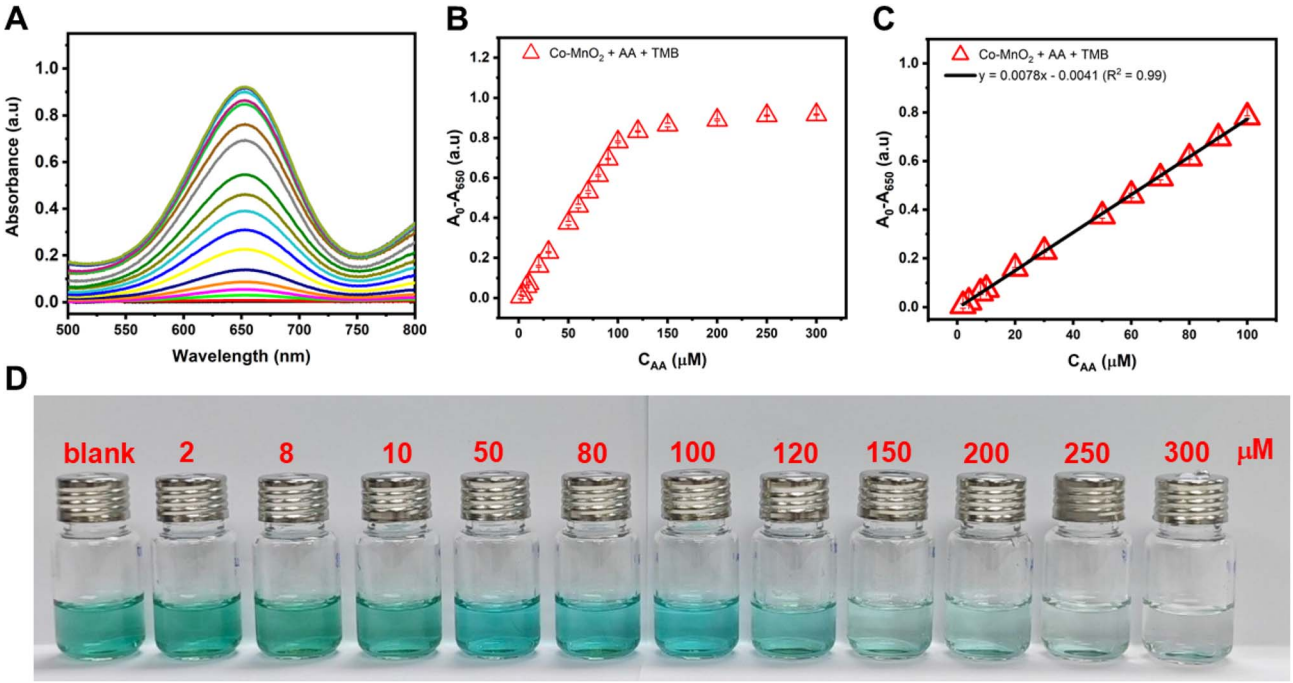

Fig. 6 (A) UV-Vis spectra of Co–MnO_2 + TMB system and (B) plot of dependence of Δ*A* on various concentrations of AA from 0 to 300 μM. (C) Colorimetric detection linear correlation for AA concentrations ranging from 2 to 100 μM. (D) Photo of vials containing Co–MnO_2 + TMB system with different AA concentrations.

doping strategy in our system was shown to enhance the overall oxidase-like activity, which is a crucial first step for a sensitive inhibition-based assay. Previous studies with Mo–MnO_2 systems proposed that nanozyme inhibition mechanisms may involve aggregation of nanoparticles and masking of active sites due to electrostatic interactions with inhibitors. While our observations primarily support a redox reaction mechanism with Mn^{4+}, further investigation into potential morphological changes or surface charge alterations of the Co–MnO_2 nanozymes upon interaction with AA could provide more comprehensive understanding of the inhibition mechanism. Notably, research by Xu *et al.* indicates that Co doping can increase oxygen vacancy concentration, which might significantly influence the interaction dynamics with TMB and AA.

3.4.2. Selectivity test. The feasibility of developing a probe is to differentiate the signal to be analyzed from other signals. To evaluate the practical applicability and selectivity of the sensor, its response to AA was tested against a range of potentially interfering species. The chosen interferents, including common metal ions ($MnCl_2$, $NiCl_2$, $CdSO_4$, $FeCl_3$) and organic molecules (D-Glucose, Acrylamide), were selected because they represent common redox-active species present in complex biological (*e.g.*, serum) and food (*e.g.*, fruit juices) matrices where AA is typically analyzed. The absorbance was measured at 650 nm after the interferents were added to the reaction system at a particular concentration (200 μM). After the interfering chemicals were added, the absorbance value changed somewhat, but for AA, the difference was evident (Fig. 7). As a result, the Co–MnO_2 + TMB system was thought to be appropriate for creating an AA detection probe.

The feasibility of developing a practical detection probe relies heavily on its ability to selectively differentiate the target analyte signal from other potentially interfering signals. To evaluate the selectivity of the Co–MnO_2 + TMB system for AA

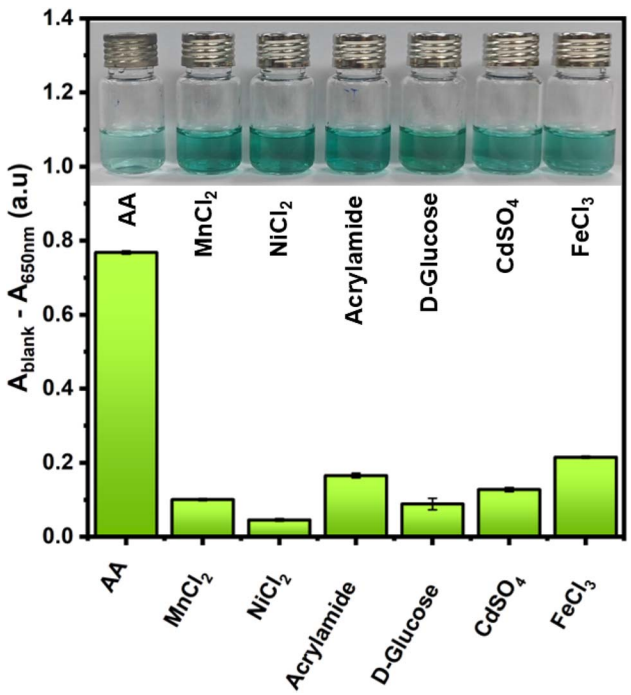

Fig. 7 Selectivity of Co–MnO_2 + TMB system for AA sensing.

Table 1 Assessment of the amount of AA included in orange fruits, tomatoes and vitamin C tablets ($n = 3$)

Sample	$C_{unspiked}$ (mM)	C_{add} (mM)	C_{spiked} (mM)			Average	STDEV	RSD (%)	Recovery (%)
			$n = 1$	$n = 2$	$n = 3$				
Orange	48.89	5	51.99	51.33	54.07	52.46	1.43	2.73	71.39
		15	64.16	63.92	66.12	64.73	1.21	1.86	105.59
		25	74.56	75.22	76.55	75.44	1.01	1.34	106.19
Tomato	22.35	5	26.11	26.77	27.15	26.67	0.53	1.98	86.6
		15	35.87	36.17	36.75	36.26	0.45	1.23	92.77
		25	48.67	48.67	48.45	48.6	0.13	0.26	105.01
AA tablet	38.05	5	42.04	43.05	42.48	42.52	0.51	1.2	89.38
		15	53.46	52.4	52.91	52.92	0.53	1.01	99.13
		25	65.47	65.68	64.03	65.06	0.9	1.38	103.89

detection, we examined its response in the presence of several additional ions and analytes. These interferents were introduced into the Co–MnO_2 + TMB reaction system at a concentration of 200 μM, and the resulting absorbance was measured at 650 nm. While some degree of absorbance change was observed upon the addition of these interfering chemicals, the change in absorbance was notably more pronounced in the presence of AA. This significant difference in response suggests that the Co–MnO_2 + TMB system possesses a certain level of selectivity towards AA, making it potentially suitable for the development of an AA detection probe.

The principle behind the AA detection in the Co–MnO_2 + TMB system, as described in the introduction, relies on the specific reduction of Mn^{4+} in Co–MnO_2 by AA to Mn^{2+}, leading to the inhibition of TMB oxidation. This specific redox reaction contributes to the observed selectivity. While other reducing agents might interact with the system to some extent, the magnitude of their effect on the Mn^{4+}/Mn^{2+} redox equilibrium and subsequently on the oxTMB formation appears less significant than that of AA, as indicated by the experimental observations. However, it is important to acknowledge that some absorbance change was observed with the interferents. This suggests that the selectivity might not be absolute, and specific compounds present in a sample matrix could potentially lead to false positive or negative results if present at sufficiently high concentrations. Further investigations involving a wider range of potential interferents relevant to the intended application of the probe and at varying concentrations would be beneficial to fully characterize the selectivity profile of the Co–MnO_2 + TMB system.

3.4.3. Detection of the AA in real sample. To assess the practical applicability of the developed Co–MnO_2 + TMB colorimetric probe, it was employed for the detection of AA in commercial medications and fruits. These samples served as representative models to evaluate the feasibility of using this method for real sample analysis. The analyte recovery results obtained from various real sample conditions are presented in Table 1. The average recovery of AA ranged from 71.39% to 106.19%, and the relative standard deviation (RSD) value was no higher than 2.73%. These findings indicate the suitability of the Co–MnO_2 + TMB method for real sample analysis.

4. Conclusions

This study successfully demonstrated the chemical synthesis of Co-doped MnO_2 nanoparticles with significantly enhanced oxidase-mimicking activity. The key to this enhancement lies in the structural and electronic modifications induced by cobalt incorporation. Specifically, Co doping promotes the formation of a high concentration of OVs and facilitates the active participation of synergistic Co^{2+}/Co^{3+} and Mn^{3+}/Mn^{4+} redox couples. The synthesized Co–MnO_2 nanoparticles showed strong affinity and superior enzyme-like activity for the TMB substrate, with kinetic analysis yielding a V_{max} of 4.69×10^{-6} M s^{-1} and a K_m of 1.17 mM. The enhanced catalytic properties were effectively applied for colorimetric detection based on the inhibition principle, where the characteristic blue color development was prevented in a concentration-dependent manner. The developed system demonstrated a linear detection range of 2–100 μM and a detection limit of 1.23 μM. The effectiveness of this colorimetric sensor was validated using real samples, confirming its practical application potential. These findings demonstrate that strategic metal doping, achieved through a cost-effective and scalable synthesis method, can significantly improve the performance of nanomaterials for diverse sensing applications, warranting further biocompatibility studies to realize their potential in fields such as biomedical diagnostics, food safety, and environmental monitoring.

Author contributions

T. H. Pham: Validation, investigation; X. D. Ngo, N. V. Tuyen and C. X. Quang: Review & editing; P. C. De: Validation, investigation T. V. Tran: Investigation, writing-original draft; N. P. D. Linh: Validation, investigation V. T. Hoang: Conceptualization, methodology, investigation, writing-review & editing; A. T. Le: Supervision, project administration.

Conflicts of interest

The authors declare that they have no known competing financial interests or personal relationships that could have appeared to influence the work reported in this paper.

Data availability

All data generated or analysed are available in this published article and its SI File. See DOI: https://doi.org/10.1039/d5ra03755g.

Acknowledgements

The authors would like to acknowledge the supports for UV-Vis from nBIORD Lab, NEB Lab (Phenikaa University), and TGA, FTIR characterization from Center for Advanced Materials and Environmental Technology. This research is funded by Vietnam National Foundation for Science and Technology Development (NAFOSTED) under grant number NCUD.01-2022.02.

References

1 L. Tian, *et al.*, Ratiometric Dual Signal-Enhancing-Based Electrochemical Biosensor for Ultrasensitive Kanamycin Detection, *ACS Appl. Mater. Interfaces*, 2020, **12**(47), 52713–52720, DOI: 10.1021/acsami.0c15898.

2 M. Jiang, X. Xu, S. Liu, L. Liu, X. Wang and H. Jiang, Enhancement of nanozyme activity by second ligand modification on glutathione protected gold nanoclusters for regulation of intracellular oxidative stress, *Inorg. Chem. Commun.*, 2024, **161**, 112115, DOI: 10.1016/J.INOCHE.2024.112115.

3 T. Sahare, N. Singh, B. N. Sahoo and A. Joshi, Smartphone-enhanced nanozyme sensors: Colorimetric and fluorescence sensing techniques, *Biosens. Bioelectron.:X*, 2024, **21**, 100544, DOI: 10.1016/J.BIOSX.2024.100544.

4 L. Zhang, F. Xin, Z. Cai, H. Zhao, X. Zhang and C. Yao, A colorimetric sensing platform for azodicarbonamide detection in flour based on MnO2 nanosheets oxidative system, *Anal. Bioanal. Chem.*, 2021, **413**(19), 4887–4894, DOI: 10.1007/S00216-021-03451-Z/METRICS.

5 Y. Liu, *et al.*, Platinum Nanoparticles: Efficient and Stable Catechol Oxidase Mimetics, *ACS Appl. Mater. Interfaces*, 2015, **7**(35), 19709–19717, DOI: 10.1021/ACSAMI.5B05180/SUPPL_FILE/AM5B05180_SI_001.PDF.

6 J. Peng and J. Weng, Enhanced peroxidase-like activity of MoS2/graphene oxide hybrid with light irradiation for glucose detection, *Biosens. Bioelectron.*, 2017, **89**, 652–658, DOI: 10.1016/J.BIOS.2015.12.034.

7 Y. Song, X. Wang, C. Zhao, K. Qu, J. Ren and X. Qu, Label-Free Colorimetric Detection of Single Nucleotide Polymorphism by Using Single-Walled Carbon Nanotube Intrinsic Peroxidase-Like Activity, *Chem.–Eur. J.*, 2010, **16**(12), 3617–3621, DOI: 10.1002/chem.200902643.

8 Y. Tao, E. Ju, J. Ren and X. Qu, Polypyrrole nanoparticles as promising enzyme mimics for sensitive hydrogen peroxide detection, *Chem. Commun.*, 2014, **50**(23), 3030–3032, DOI: 10.1039/C4CC00328D.

9 L. Feng, *et al.*, An Ultrasmall SnFe2O4 Nanozyme with Endogenous Oxygen Generation and Glutathione Depletion for Synergistic Cancer Therapy, *Adv. Funct. Mater.*, 2021, **31**(5), 2006216, DOI: 10.1002/ADFM.202006216.

10 S. Li, X. Zhao, R. Gang, B. Cao and H. Wang, Doping Nitrogen into Q-Graphene by Plasma Treatment toward Peroxidase Mimics with Enhanced Catalysis, *Anal. Chem.*, 2020, **92**(7), 5152–5157, DOI: 10.1021/ACS.ANALCHEM.9B05645/SUPPL_FILE/AC9B05645_SI_001.PDF.

11 A. Raj, R. M. Rego, K. V. Ajeya, H.-Y. Jung and M. D. Kurkuri, Basil seeds loaded with MOFs as an eco-friendly and sustainable adsorbent for efficient removal of hazardous organic pollutants from water, *Sep. Purif. Technol.*, 2024, **330**, 125370, DOI: 10.1016/j.seppur.2023.125370.

12 Y. Meng, *et al.*, Effects of crystal structure on the activity of MnO2 nanorods oxidase mimics, *Nano Res.*, 2020, **13**(3), 709–718, DOI: 10.1007/S12274-020-2680-5/METRICS.

13 H. Lin, D. Chen, H. Liu, X. Zou and T. Chen, Effect of MnO2 crystalline structure on the catalytic oxidation of formaldehyde, *Aerosol Air Qual. Res.*, 2017, **17**(4), 1011–1020, DOI: 10.4209/aaqr.2017.01.0013.

14 Z. Ali, R. Ullah, M. Tuzen, S. Ullah, A. Rahim and T. A. Saleh, Colorimetric sensing of heavy metals on metal doped metal oxide nanocomposites: A review, *Trends Environ. Anal. Chem.*, 2023, **37**, e00187, DOI: 10.1016/J.TEAC.2022.E00187.

15 Y. Sun, *et al.*, Integration of Manganese Dioxide-Based Nanomaterials for Biomedical Applications, *Adv. NanoBiomed Res.*, 2023, **3**(1), 2200093, DOI: 10.1002/ANBR.202200093.

16 Y. Wan, P. Qi, D. Zhang, J. Wu and Y. Wang, Manganese oxide nanowire-mediated enzyme-linked immunosorbent assay, *Biosens. Bioelectron.*, 2012, **33**(1), 69–74, DOI: 10.1016/J.BIOS.2011.12.033.

17 B. Chen, B. Wu, L. Yu, M. Crocker and C. Shi, Investigation into the Catalytic Roles of Various Oxygen Species over Different Crystal Phases of MnO2for C6H6and HCHO Oxidation, *ACS Catal.*, 2020, **10**(11), 6176–6187, DOI: 10.1021/acscatal.0c00459.

18 H. Wang, *et al.*, Construction of K and Tb Co-doped MnO2 nanoparticles for enhanced oxidation and detoxication of organic dye waste, *Chemosphere*, 2022, **297**, 134104, DOI: 10.1016/J.CHEMOSPHERE.2022.134104.

19 Y. Lian, X. Yuan, Y. Wang and L. Wei, Highly sensitive visual colorimetric sensor for xanthine oxidase detection by using MnO2-nanosheet-modified gold nanoparticles, *Spectrochim. Acta Part A Mol. Biomol. Spectrosc.*, 2022, **276**, 121219, DOI: 10.1016/J.SAA.2022.121219.

20 Z. Liang, Z. Chen, Y. Xu, H. Wang, L. Zhou and B. Yan, Sustainable production of Fe-doped MnO2 nanoparticles for accelerated tetracycline antibiotic detoxification, *Chemosphere*, 2023, **344**, 140353, DOI: 10.1016/J.CHEMOSPHERE.2023.140353.

21 X. Chen, *et al.*, Oxygen Vacancy-Rich Cobalt-Doped MnO 2 Nanorods for Zn Ion Batteries, *ACS Appl. Mater. Interfaces*, 2025, **17**(8), 12074–12084, DOI: 10.1021/acsami.4c19746.

22 A. Yusuf, *et al.*, Opposite Effects of Co and Cu Dopants on the Catalytic Activities of Birnessite MnO 2 Catalyst for Low-Temperature Formaldehyde Oxidation, *J. Phys. Chem. C*, 2020, **124**(48), 26320–26331, DOI: 10.1021/acs.jpcc.0c08508.

23 X. Wang, *et al.*, Enhanced oxidase-like activity of Mo-MnO2 nanozymes for colorimetric sensing of isoniazid and ascorbic acid, *Colloids Surf., A*, 2025, **708**, 136040, DOI: 10.1016/J.COLSURFA.2024.136040.

24 W. Shi, X. Wang, Z. Yang, J. Yang, X. Fu and X. Wang, Sr-doped MnO2 with enhanced dual-enzyme mimetic activity for colorimetric detection of glutathione and 2,4-dichlorophenol, *Microchem. J.*, 2025, **212**, 113166, DOI: 10.1016/J.MICROC.2025.113166.

25 Q. Lian, X. Zheng, G. Peng, Z. Liu, L. Chen and S. Wu, Oxidase Mimicking of CuMnO2 Nanoflowers and the Application in Colorimetric Detection of Ascorbic Acid, *Colloids Surf., A*, 2022, **652**, 129887, DOI: 10.1016/J.COLSURFA.2022.129887.

26 L. Xu, *et al.*, Co-doped MnO2 with abundant oxygen vacancies as a cathode for superior aqueous magnesium ion storage, *Inorg. Chem. Front.*, 2023, **10**(6), 1748–1757, DOI: 10.1039/D2QI02380F.

27 P. Patra, S. Laha and S. Ghosh, Exfoliated Cobalt-Doped Manganese Oxide Nanosheets: An Efficient and Stable Electrocatalyst for Hydrogen Evolution Reaction in an Alkaline Medium, *ACS Appl. Energy Mater.*, 2024, **7**(9), 3577–3589, DOI: 10.1021/ACSAEM.3C03022/SUPPL_FILE/AE3C03022_SI_001.PDF.

28 F. Li, *et al.*, Flexible microfluidic colorimetric detection chip integrated with ABTS·+ and Co@MnO2 nanozyme catalyzed TMB reaction systems for bio-enzyme free detection of sweat uric acid, *Anal. Chim. Acta*, 2024, **1299**, 342453, DOI: 10.1016/J.ACA.2024.342453.

29 M. V. Parmekar and A. V. Salker, Highly tuned cobalt-doped MnO2 nanozyme as remarkably efficient uricase mimic, *Appl. Nanosci.*, 2020, **10**(1), 317–328, DOI: 10.1007/S13204-019-01118-X/METRICS.

30 C. Stella, N. Soundararajan and K. Ramachandran, Structural, optical, dielectric and magnetic properties of Mn 1-xCoxO2 nanowires, *Superlattices Microstruct.*, 2014, **71**, 203–210, DOI: 10.1016/J.SPMI.2014.03.044.

31 R. D. Shannon, Revised effective ionic radii and systematic studies of interatomic distances in halides and chalcogenides, *Acta Crystallogr., Sect. A*, 1976, **32**(5), 751–767, DOI: 10.1107/S0567739476001551.

32 D. Jampaiah, *et al.*, Nanowire Morphology of Mono- and Bidoped α-MnO 2 Catalysts for Remarkable Enhancement in Soot Oxidation, *ACS Appl. Mater. Interfaces*, 2017, **9**(38), 32652–32666, DOI: 10.1021/acsami.7b07656.

33 K. D. Kwon, K. Refson and G. Sposito, Understanding the trends in transition metal sorption by vacancy sites in birnessite, *Geochim. Cosmochim. Acta*, 2013, **101**, 222–232, DOI: 10.1016/j.gca.2012.08.038.

34 R. M. Rego, *et al.*, Nanoarchitectonics of Bimetallic MOF@Lab-Grade Flexible Filter Papers: An Approach Towards Real-Time Water Decontamination and Circular Economy, *Small*, 2023, **19**(45), 2302692, DOI: 10.1002/smll.202302692.

35 T. H. Pham, *et al.*, Unveiling the role of heterophase nanostructure in MnO2-based colorimetric sensors for ascorbic acid detection, *Microchim. Acta*, 2024, **191**(9), 1–10, DOI: 10.1007/S00604-024-06598-5/METRICS.

36 J. Wang, *et al.*, Superfine MnO 2 Nanowires with Rich Defects Toward Boosted Zinc Ion Storage Performance, *ACS Appl. Mater. Interfaces*, 2020, **12**(31), 34949–34958, DOI: 10.1021/acsami.0c08812.

37 P.-L. Lan, I.-C. Ni, C.-I. Wu, C.-C. Hsu, I.-C. Cheng and J.-Z. Chen, Ultrafast Fabrication of H2SO4, LiCl, and Li2SO4 Gel Electrolyte Supercapacitors with Reduced Graphene Oxide (rGO)-LiMnOx Electrodes Processed Using Atmospheric-Pressure Plasma Jet, *Micromachines*, 2023, **14**(9), 1701, DOI: 10.3390/mi14091701.

38 H. Xu, *et al.*, High-loading Co-doped NiO nanosheets on carbon-welded carbon nanotube framework enabling rapid charge kinetic for enhanced supercapacitor performance, *J. Energy Chem.*, 2020, **50**, 240–247, DOI: 10.1016/j.jechem.2020.03.023.